Recent progress in anomalous Hall and Nernst effects in rare-earth ferromagnets RMn_2Ge_2

Chen Hu(胡晨), Baomin Wang(王保敏)

Citation: Chin. Phys. B. 35, 107503 (2026). DOI: 10.1088/1674-1056/ae9a5b | CSTR: 32038.14.CPB.ae9a5b
http://cpb.iphy.ac.cn; http://iopscience.iop.org/cpb

What follows is a list of articles you may be interested in

Data driven structure property relationship and rational design of rare-earth magnetostrictive materials

Dan Liu(刘丹), Ying Tong(童颖), Yuan Li(李渊), Xinqi Zheng(郑新奇), Qiong Wu(吴琼), Ruoshui Liu(刘若水), Xin Ming(明昕), Yinong Yin(尹亦农), Jianfeng Xi(息剑峰), Tongyun Zhao(赵同云), Fengxia Hu(胡凤霞), Baogen Shen(沈保根)

Chin. Phys. B. 35, 097505 (2026). DOI: 10.1088/1674-1056/ae9a57 | CSTR: 32038.14.CPB.ae9a57

Enhanced low-field magnetocaloric effect induced by Co doping in $RCu_{2-x}Co_x$ (R = Er, Ho) compounds for liquid hydrogen

Lu Tian(田路), Zhaojun Mo(莫兆军), Xuanyu Qiao(乔轩雨), Chenyang Ma(马辰洋), Guodong Liu(刘国栋)

Chin. Phys. B. 35, 077505 (2026). DOI: 10.1088/1674-1056/ae360a | CSTR: 32038.14.CPB.ae360a

Review of the strategies for regulating working temperatures of rare-earth-based low temperature magnetic cooling materials

Jie Zhao(赵洁), Yawei Gao(高亚伟), Dingsong Wang(王鼎淞), Shuxian Yang(杨淑娴), Lei Xi(奚磊), Hao Liu(刘昊), Yang Pan(潘洋), Jiawang Xu(许家旺), Xinqi Zheng(郑新奇), Shouguo Wang(王守国)

Chin. Phys. B. 35, 077501 (2026). DOI: 10.1088/1674-1056/ae3f92 | CSTR: 32038.14.CPB.ae3f92

Wideband near-infrared emission from $GaScO_3:Cr^{3+}$ phosphors with a perovskite structure

Chong Li(李翀), Mengyu Zhang(张梦宇), Chuancheng Zhang(张传成), Wenzhi Su(宿文志), Yong Zou(邹勇), Shoujun Ding(丁守军), Qingli Zhang(张庆礼)

Chin. Phys. B. 34, 087502 (2025). DOI: 10.1088/1674-1056/add506 | CSTR: 32038.14.CPB.add506

Enhanced anomalous Hall effect in kagome magnet $YbMn_6Sn_6$ with intermediate-valence ytterbium

Longfei Li(李龙飞), Shengwei Chi(迟晟玮), Wenlong Ma(马文龙), Kaizhen Guo(郭凯臻), Gang Xu(徐刚), Shuang Jia(贾爽)

Chin. Phys. B. 33, 057501 (2024). DOI: 10.1088/1674-1056/ad322d

---

TOPICAL REVIEW — A 40th Anniversary Celebration: Physics Research and Innovation at Ningbo University

Recent progress in anomalous Hall and Nernst effects in rare-earth ferromagnets $R\mathrm{Mn_2Ge_2}$

Chen Hu(胡晨) and Baomin Wang(王保敏)[†]

School of Physical Science and Technology, Ningbo University, Ningbo 315211, *China*

(Received 27 May 2026; revised manuscript received 4 August 2026; accepted manuscript online 17 August 2026)

Anomalous transverse transport phenomena include two major effects. One is the anomalous Hall effect (AHE). The other is the anomalous Nernst effect (ANE). It is an important probe of the interplay among magnetic order, spin–orbit coupling (SOC), and electronic structure in magnetic materials. Rare-earth-based $R\mathrm{Mn_2Ge_2}$ ferromagnets, due to their unique layered structure, tunable magnetism, and complex electronic behavior, have emerged as an important platform for studying these transport phenomena. This paper reviews recent research progress in the ferromagnetic $R\mathrm{Mn_2Ge_2}$ (R = La, Ce, Pr, Nd, Sm) system in the study of AHE and ANE, analyzes the modulation of these effects by different rare-earth elements, and discusses the relationship between these effects and magnetic and electronic structures. Recent studies suggest that by adjusting the magnetic structure, the response of these transverse transport phenomena can be significantly altered, providing new directions for the application of low-power electronic devices and energy conversion technologies.

Keywords: rare-earth compounds, transverse transport, anomalous Hall effect, anomalous Nernst effect, magnetic materials, thermoelectric properties

PACS: 75.50.Cc, 72.15.Gd, 72.20.Pa, 75.25–j

DOI: 10.1088/1674-1056/ae9a5b **CSTR:** 32038.14.CPB.ae9a5b

1. Introduction

With the development of low-power electronic devices and energy-conversion technologies, transverse transport phenomena involving coupled transport of spin, charge, and heat have become a research focus. In magnetic materials, two representative transverse transport phenomena are commonly observed. One is the anomalous Hall effect (AHE). The other is the anomalous Nernst effect (ANE).[1] The AHE describes transverse charge transport that is driven by a longitudinal charge current. The ANE is generated by a temperature gradient. Recent studies have shown that the strengths of the AHE and ANE cannot be explained solely by the macroscopic magnetic moment. By contrast, these responses are governed by multiple factors. These factors include crystal symmetry, magnetic structure, and the electronic states near the Fermi level. The AHE is closely associated with Berry curvature. Specifically, it reflects the Berry curvature integrated over the occupied states.[2] Conversely, the ANE is more sensitive to Berry curvature. In particular, it is strongly affected by the energy dependence near the Fermi level. Consequently, anomalous transverse transport phenomena serve as an important probe of the electronic structure of topological magnets and complex magnetic materials.

$R\mathrm{Mn_2Ge_2}$ (R denotes a rare-earth element) is a representative series of layered Mn-based intermetallics.[3,4] These compounds crystallize in the $\mathrm{ThCr_2Si_2}$-type body-centered tetragonal structure. In this structure, Mn atoms are arranged in a square lattice within the *ab* plane. Along the *c* axis, these Mn layers alternate with Ge layers and rare-earth-element layers, as shown in Fig. 1(a). This layered framework renders the intralayer and interlayer exchange interactions within the Mn sublattice highly sensitive to the lattice parameters and interatomic distances, thereby providing the structural basis for the formation, competition, and transformation of various magnetic orders.[5] Thus, $R\mathrm{Mn_2Ge_2}$ can be better described as a multiphase magnetic system governed by structural parameters, exchange competition, and magnetocrystalline anisotropy, rather than as a single conventional ferromagnet.

Variations in the rare-earth element can significantly affect the magnetic ground states and the anomalous transverse transport properties of $R\mathrm{Mn_2Ge_2}$. In this review, we focus on the light rare-earth elements, namely R = La,[6,9–16] Ce,[7,17–21] Pr,[7,22–28] Nd,[7,29–35] and Sm.[8,36–41] Previous studies have shown that these compounds tend to exhibit ferromagnetic phases across a wide temperature range. This feature renders them more suitable for comparative studies of AHE and ANE. Conversely, many of the remaining rare-earth elements exhibit predominantly antiferromagnetic phases, and their anomalous transverse transport is less directly relevant to the focus of this review.

Although these light rare-earth elements are often regarded as ferromagnetic systems, they do not usually exhibit

[†]Corresponding author. E-mail: wangbaomin@nbu.edu.cn

© 2026 Chinese Physical Society and IOP Publishing Ltd. All rights, including for text and data mining, AI training, and similar technologies, are reserved.

simple collinear ferromagnetism. The Mn sublattices in these compounds typically display canted or conical noncollinear magnetic structures.

$LaMn_2Ge_2$[6] and $CeMn_2Ge_2$[7] exhibit an intralayer antiferromagnetic (AFM) state at high temperatures, and also transform into the conical ferromagnetic structure (FMconical) phase upon further cooling as shown in Fig. 1(b). As the temperature decreases, $PrMn_2Ge_2$[7] undergoes a sequence of magnetic phase transitions, as illustrated in Fig. 1(c). The system first enters an AFM state, followed by a ferromagnetic phase (FM). Upon further cooling, the Mn sublattice develops the FMconical structure. At lower temperatures, the Mn sublattice retains this conical ordering, while the Pr sublattice becomes ferromagnetically ordered along the c axis (FMPr). Consequently, the two magnetically ordered sublattices coexist in the low-temperature phase. With decreasing temperature, $NdMn_2Ge_2$[7] exhibits a successive evolution of magnetic phases, as shown in Fig. 1(d). The system first enters an AFM state, followed by a canted ferromagnetic state in which the Mn sublattice contains antiferromagnetic components within the layers and a FM component along the c axis. Upon further cooling, the Mn sublattice transforms into a FMconical, characterized by spiral antiferromagnetic components within the layers accompanied by ferromagnetism oriented along the c direction. At the lowest temperatures, the Mn sublattice remains conically ordered; however, the spiral antiferromagnetic components reorient into the ac plane, while the ferromagnetic component switches to the b axis (FMb). Simultaneously, the Nd sublattice becomes ferromagnetically ordered (FMNd), with its magnetic moments aligned along the b axis. $SmMn_2Ge_2$ exhibits even more complex magnetic phenomena.[8] It exhibits a high-temperature FM phase, a predominantly AFM intermediate phase, and a low-temperature reentrant ferromagnetic (RFM) phase, as shown in Fig. 1(e). In summary, the common feature of light rare-earth RMn_2Ge_2 is not simple ferromagnetic alignment, but ferromagnetism-related noncollinear magnetic order.

The light rare-earth RMn_2Ge_2 compounds exhibit a combination of layered crystal structures, complex magnetic phase evolution, and ferromagnetism-associated noncollinear magnetic order. Along with the pronounced member-dependent differences in AHE and ANE responses, these features render them a suitable platform for investigating the cooperative influence of structure, magnetism, and electronic structure on anomalous transverse transport. This article summarizes newly reported developments concerning the AHE and ANE of light rare-earth RMn_2Ge_2 compounds. The discussion focuses especially on the effect of rare-earth elements on anomalous transverse transport.

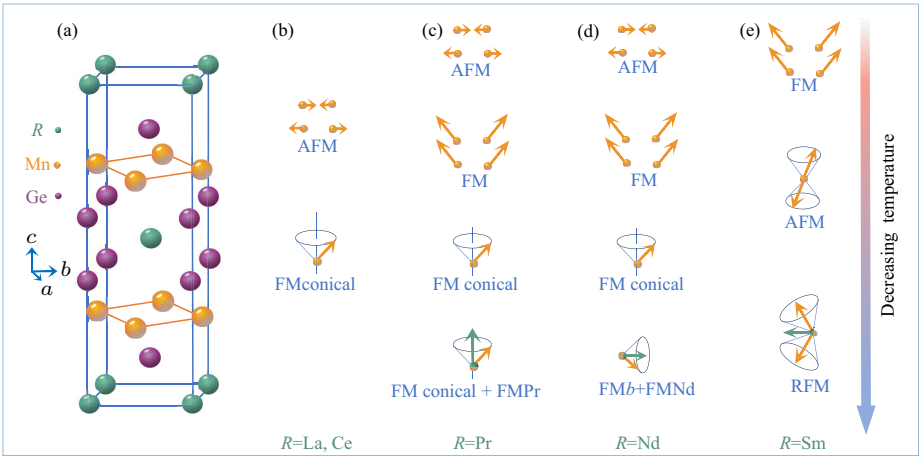

Fig. 1. Schematic illustration of the crystal structure and magnetic configuration of RMn_2Ge_2: (a) crystal structure, the magnetic moments of the R atoms are represented by the green arrows, whereas orange arrows represent those of the Mn atoms. Temperature-dependent magnetic phase diagrams of (b) $LaMn_2Ge_2$,[6] (c) $PrMn_2Ge_2$,[7] (d) $NdMn_2Ge_2$,[7] and (e) $SmMn_2Ge_2$.[8]

2. Theoretical framework and transport mechanisms of the AHE

AHE is a typical transverse transport phenomenon in magnetic materials. The schematic diagram is illustrated in Fig. 2. Unlike the ordinary Hall effect driven by an external magnetic field, the AHE may arise from internal magnetic order even without an external magnetic field. Its emergence typically relies on the violation of time-reversal symmetry and is intimately associated with spin–orbit coupling (SOC). Because the AHE is highly sensitive to the electronic structure, band geometry, and scattering mechanisms, it has become an important probe of transport properties and topological band features in magnetic systems.[42–45]

The anomalous Hall resistivity ρ_{yx}^{A} is defined by

$$\rho_{yx}^{A} = E_y/J_x. \tag{1}$$

Here, E_y denotes the transverse electric field, whereas J_x represents the longitudinal current density. In conventional ferromagnets, the anomalous term is often approximated by

$$\rho_{yx}^{A} = R_s\mu_0 M_z. \tag{2}$$

Here, R_s denotes the anomalous Hall coefficient. μ_0 stands for the vacuum permeability. M_z represents the z component of the magnetization. This decomposition is primarily an empirical formula employed in experimental analysis and does not imply a strict one-to-one correspondence between the AHE and the net magnetization. In multiband systems, noncollinear magnets, and topological magnetic materials, the anomalous Hall response is often governed jointly by the band structure, crystal symmetry, and scattering processes.

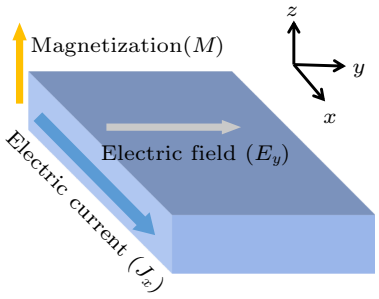

Fig. 2. Schematic illustration of AHE.

Within the linear-response framework, the AHE is more commonly characterized by the anomalous Hall conductivity (AHC) σ_{yx}^{A}:

$$J_y = \sigma_{yx}^{\mathrm{A}} E_x. \tag{3}$$

Here, J_y denotes the transverse current density. E_x represents the longitudinal electric field. In experiments, the Hall resistivity is usually measured directly, so a tensor conversion is required when comparing experimental data with theoretical results. In the common case,

$$\sigma_{yx}^{\mathrm{A}} = -\frac{\rho_{yx}^{\mathrm{A}}}{\rho_{xx}\rho_{yy} + \left(\rho_{yx}^{\mathrm{A}}\right)^2}. \tag{4}$$

Here, ρ_{xx} and ρ_{yy} are the longitudinal resistivity along the x and y directions. From a microscopic standpoint, the AHE is generally considered to contain contributions of intrinsic and extrinsic origin. The intrinsic component originates from the Berry curvature of the electronic bands. The corresponding AHC can be written as the integral of the Berry curvature over the occupied states in the Brillouin zone. As a result, it is highly sensitive to band regions near the Fermi level. In these regions, the Berry curvature is strongly enhanced, such as near Weyl nodes, avoided band crossings, and regions with small band gaps.[46,47] The assertion that the intrinsic part remains unaffected by the scattering time merely indicates that its physical origin differs from that of impurity-induced extrinsic scattering. It does not mean that the experimentally measured Hall signal is completely unaffected by temperature, disorder, or multiband effects. In practice, identifying the intrinsic mechanism still requires a combined analysis of transport measurements and electronic structure calculations. In addition to the intrinsic contribution, extrinsic contributions to the AHE may also originate from impurity scattering in the presence of SOC. The principal extrinsic mechanisms include skew scattering[48] and the side-jump mechanism.[49] Skew scattering originates from the unequal probabilities of leftward and rightward scattering. That is, in the presence of SOC, impurity potentials deflect electrons unequally toward two opposite transverse directions. After statistical averaging, this imbalance leads to a finite net transverse current. This mechanism is therefore more important in clean samples with high conductivity and low disorder. By contrast, the side-jump mechanism does not rely on asymmetric scattering probabilities, but instead originates from the lateral shift of the electron wave packet during a single scattering process. In real materials, the AHE is often determined by the combined effects of intrinsic, skew-scattering, and side-jump contributions.

Experimentally, a common way to distinguish different mechanisms is to analyze the empirical dependence of anomalous Hall resistivity on longitudinal resistivity:

$$\rho_{yx}^{\mathrm{A}} \propto \rho_{xx}^{a}. \tag{5}$$

It is generally believed that, in the relatively clean limit, $a \approx 1$ indicates a dominant skew-scattering contribution, whereas $a \approx 2$ is more often associated with intrinsic or side-jump-dominated behavior. However, this scaling relation is an empirical criterion rather than a strict theorem. In the presence of multiband transport, strong disorder, pronounced localization effects, or significant temperature-induced band reconstruction, the simple power-law relation may deviate substantially or even break down.

The dominant AHE mechanism is strongly material dependent. In conventional ferromagnetic metals, intrinsic and extrinsic contributions usually coexist, and their relative weights can be redistributed by sample purity, temperature, and transport conditions. By contrast, in topological magnets, magnetic Weyl semimetals, and some noncollinear antiferromagnets, the Berry curvature-driven intrinsic mechanism is often more prominent. For the $R\mathrm{Mn_2Ge_2}$ system, the physical origin of the AHE likewise cannot be simply attributed to a single mechanism, but should be analyzed in light of its specific magnetic structure, electronic structure, and transport behavior.

3. Theoretical framework and transport mechanisms of the ANE

In magnetic systems, a longitudinal temperature gradient can induce a transverse electric field. This phenomenon is called the ANE. The schematic diagram is illustrated in Fig. 3. Unlike the conventional Nernst effect, which requires

a magnetic field emerging from an external origin, the ANE may originate from the intrinsic magnetic order of the system, without the application of an external field.[50] Its occurrence generally requires broken time-reversal symmetry and is closely associated with SOC. Because the ANE is highly sensitive to the electronic structure, band geometry, and scattering processes, it has become an important probe of transverse thermoelectric transport in magnetic materials.

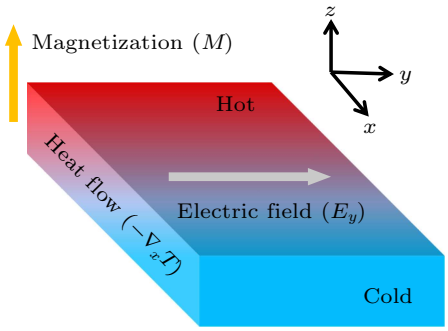

Fig. 3. Schematic illustration of ANE.

Under open-circuit conditions, the anomalous Nernst signal is defined as

$$S_{yx}^{\mathrm{A}} = \frac{E_y}{\nabla_x T}. \tag{6}$$

Here, $\nabla_x T$ denotes the temperature gradient imposed along the x direction. Under an external magnetic field, the conventional Nernst background must first be separated from the anomalous contribution before turning to the physical meaning of the anomalous component S_{yx}^{A}. In multiband systems, noncollinear magnets, and topological magnetic materials, the magnitude of the transverse thermoelectric signal cannot be inferred solely from the net magnetization. As long as a pronounced Berry curvature distribution exists near the Fermi level,[51,52] a sizable transverse response can arise even when the net magnetic moment is relatively small.

ANE measurements are highly sensitive to the measurement geometry and temperature distribution. For thin-film samples, heat conduction through the substrate and interfacial thermal resistance can strongly affect the effective thermal gradient across the sample interior. For single-crystal samples, the relation between the measurement direction and the crystallographic axes must be clearly specified, especially in low-symmetry or anisotropic systems. In these cases, the extracted S_{yx}^{A} under different configurations corresponds to distinct components of the anomalous thermoelectric transport tensor. In addition, the longitudinal Seebeck signal can contribute to the transverse channel due to electrode misalignment or an inhomogeneous temperature field, resulting in an overestimation of the ANE.[53] Reliable ANE measurements therefore require not only good signal reproducibility, but also systematic checks of the temperature distribution, polarity reversal, background symmetry, and geometric errors.

In transport analysis, S_{yx}^{A} is not equivalent to a single anomalous transverse thermoelectric conductivity (ANC) component. Under open-circuit conditions, the anomalous transverse thermoelectric signal can be written as

$$S_{yx}^{\mathrm{A}} = \rho_{yx}^{\mathrm{A}}\alpha_{xx} + \rho_{yy}\alpha_{yx}^{\mathrm{A}}. \tag{7}$$

Here α_{xx} and α_{yx}^{A} are the longitudinal and ANC components. This expression indicates that the anomalous transverse thermoelectric signal arises from the coupled contributions of thermoelectric and electrical transport, rather than directly reflecting a single transport coefficient. Here, $\rho_{yy}\alpha_{yx}^{\mathrm{A}}$ represents the direct contribution of α_{yx}^{A}, whereas $\rho_{yx}^{\mathrm{A}}\alpha_{xx}$ describes the correction induced by the longitudinal thermoelectric response through the anomalous Hall channel. Therefore, even when different samples have similar α_{yx}^{A}, S_{yx}^{A} can still differ significantly because of differences in ρ_{yy}, ρ_{yx}^{A}, or α_{xx}. When comparing ANE responses in different materials, S_{yx}^{A}, α_{yx}^{A}, ρ_{yy}, and ρ_{yx}^{A} should be analyzed within a unified transport framework.

From a microscopic perspective, the ANE and the AHE share a common geometric origin, since both are related to Berry curvature. However, they emphasize different aspects of the electronic structure. The AHE is more directly associated with the cumulative contribution of occupied states to transverse charge transport. In contrast, the ANE is more sensitive to the Berry curvature distribution in the vicinity of the Fermi level. As a result, the ANE is more effective in amplifying fine band features near the Fermi level, such as regions around Weyl nodes, avoided band crossings, and Berry curvature-enhanced regions near small band gaps. In the low-temperature and degenerate limit, the relation between the ANE and the AHE is often described by the generalized Mott relation

$$\alpha_{yx}^{\mathrm{A}} = -\frac{\pi^2 k_{\mathrm{B}}^2 T}{3e}\frac{\partial \sigma_{yx}^{\mathrm{A}}}{\partial E}\bigg|_{E=E_{\mathrm{F}}}. \tag{8}$$

Moreover, k_{B} represents the Boltzmann constant. T is the absolute temperature. e denotes the elementary charge. And E_{F} is the Fermi level. Under the coordinate convention adopted here, the transverse anomalous component is described by the relation between α_{yx}^{A} and σ_{yx}^{A}. This equation shows that the anomalous transverse thermoelectric conductivity is not determined directly by the AHC itself, but mainly by its energy derivative near the Fermi level.[54] Therefore, even if the AHE amplitude is not particularly large in a given material, a pronounced ANE signal may still emerge provided that σ_{yx}^{A} exhibits a strong energy dependence in the vicinity of the Fermi level.

Besides the intrinsic geometric mechanism, the ANE can also receive contributions from extrinsic scattering. Similar to the AHE, skew scattering originates from the asymmetry of the scattering probability, whereas the side-jump mechanism is

associated with the transverse coordinate shift during the scattering process. Their relative weights are not fixed across different disorder strengths or transport regimes. Therefore, the ANE in real materials is often the result of the combined action of the intrinsic Berry curvature effect and extrinsic scattering processes, rather than a pure manifestation of a single mechanism. Accordingly, the physical origin of the ANE should not be judged solely from a single temperature point or a single peak value. Instead, it should be analyzed together with the resistivity, Hall response, thermoelectric conductivity, and electronic structure calculations.

Overall, the ANE connects thermoelectric transport, charge transport, and band geometry within a unified framework. Compared with the AHE, it is more sensitive to the energy dependence of the Berry curvature in the vicinity of the Fermi level. This gives the ANE a unique advantage in revealing subtle band reconstructions and clarifying the origin of transverse thermoelectric responses. For the RMn$_2$Ge$_2$ system, the physical origin of the ANE likewise cannot be simply attributed to a single mechanism. Instead, it should be understood in light of the specific magnetic structure, electronic structure, and transport background of the material.

4. AHE and related phenomena in RMn$_2$Ge$_2$ ferromagnets

The light rare-earth intermetallic RMn$_2$Ge$_2$ family exhibits rich magnetic structures and strong anisotropic interactions, making it an excellent platform for studying the AHE. Different rare-earth elements modify the magnetic ground state and lead to distinct low-temperature spin configurations as well as different temperature-driven magnetic transitions. These variations in magnetic order directly affect transverse charge transport and provide a basis for analyzing the respective intrinsic and extrinsic terms of the AHE. This section reviews experimental and theoretical studies on LaMn$_2$Ge$_2$,[9,10] CeMn$_2$Ge$_2$,[17] PrMn$_2$Ge$_2$,[22,27,28] NdMn$_2$Ge$_2$,[29,32] and SmMn$_2$Ge$_2$,[36,40] with emphasis on the interplay among magnetic structure, measurement geometry, and temperature-dependent scaling behavior.

4.1. LaMn$_2$Ge$_2$

Gong *et al.*[9] measured the Hall response in LaMn$_2$Ge$_2$ single crystals under $H \parallel c$ and $I \parallel a$ as shown in Fig. 4(a). To suppress electrode misalignment and longitudinal-signal mixing, the data were antisymmetrized with respect to positive and negative magnetic fields and then converted into the σ_{xy}^{A} using the longitudinal resistivity. At 10 K, σ_{xy}^{A} reaches approximately 730 $\Omega^{-1}\cdot$cm^{-1} as shown in Fig. 4(b). It decreases gradually with increasing temperature but remains substantial. The isothermal ρ_{xy} closely follows the magnetization curve, indicating that the anomalous term dominates.

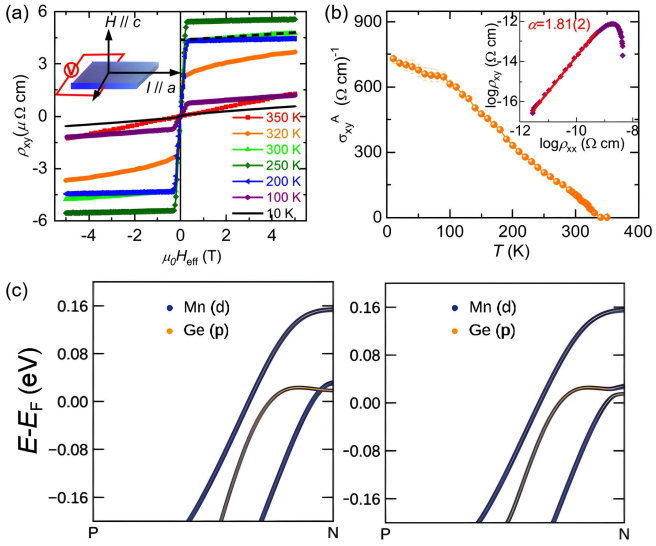

Fig. 4. Experimental results and intrinsic mechanism of the AHE in LaMn$_2$Ge$_2$. (a) Magnetic-field-dependent Hall resistivity;[9] (b) σ_{xy}^{A} and scaling relation;[9] (c) Berry curvature contribution induced by Mn-d and Ge-p orbital hybridization.[10]

Power-law scaling, $\rho_{xy}^{A} \propto \rho_{xx}^{a}$, gives $a \approx 1.81$ as shown in Fig. 4(b). This value is close to quadratic scaling and suggests that the low-temperature AHE is predominantly intrinsic and governed by Berry curvature. Roychowdhury *et al.*[10] further combined angle-resolved transport, single-crystal neutron diffraction, together with the first-principles calculations presented in Fig. 4(c). They linked the experimental peak response to Berry curvature hotspots arising from Mn-d and Ge-p hybridization near the Fermi level. Together, these studies establish the intrinsic source of the low-temperature AHE in LaMn$_2$Ge$_2$ and connect the transport response with its electronic structure.

4.2. CeMn$_2$Ge$_2$

CeMn$_2$Ge$_2$ undergoes antiferromagnetic ordering at 394 K and forms a conical spin state at low temperatures. Xu *et al.*[17] measured ρ_{xy} in single crystals under $H \parallel c$ and $I \parallel a$ as shown in Fig. 5(a). The data were antisymmetrized under

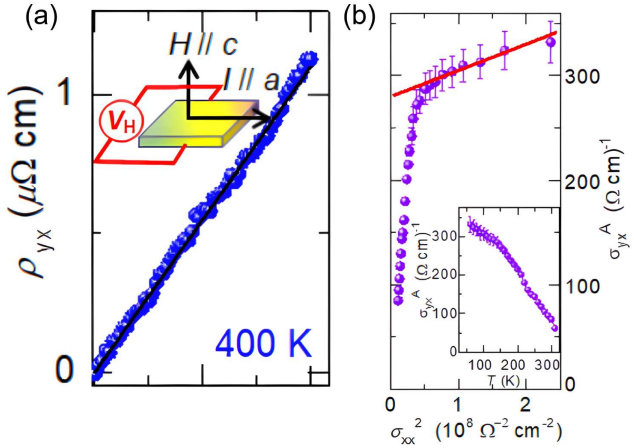

Fig. 5. Measurement configuration and intrinsic contribution of the AHE in CeMn$_2$Ge$_2$.[17] (a) Hall-effect measurement configuration and magnetic-field-dependent Hall resistivity; (b) intrinsic σ_{xy}^{A} obtained from TYJ scaling analysis.

field reversal and converted into σ_{xy}^{A}. As shown in Fig. 5(b), the peak low-temperature value of σ_{xy}^{A} is approximately 276 $\Omega^{-1}\cdot cm^{-1}$. This suggests that the anomalous contribution is the dominant component of the Hall response. Analysis based on the Tian–Ye–Jin (TYJ) scaling relation, $\sigma_{xy}^{A} = \alpha\sigma_{xx}^{2} + \sigma_{xy}^{int}$, shows that the intrinsic contribution accounts for about 81% of the total response as shown in Fig. 5(b). Combined with magnetic characterization, transport fitting, and TYJ scaling analysis, these results indicate that the low-temperature AHE in $CeMn_2Ge_2$ is mainly intrinsic.

4.3. $PrMn_2Ge_2$

Wang *et al.*[28] measured ρ_{xy}^{A} in $PrMn_2Ge_2$ single crystals under $H \parallel c$ and $I \parallel a$, obtaining a low-temperature σ_{xy}^{A} of about 220 $\Omega^{-1}\cdot cm^{-1}$ as shown in Fig. 6(a). The power-law exponent $a \approx 1.18$ indicates that skew scattering dominates at low temperatures. Abrupt jumps in the low-temperature magnetic hysteresis loops are accompanied by corresponding changes in the Hall resistivity, showing that domain dynamics affect charge transport. Huang *et al.*[27] extended the measurements to different field and current orientations. For $H \parallel c$, σ_{xy}^{A} reaches about 300 $\Omega^{-1}\cdot cm^{-1}$ at low temperatures. When an in-plane magnetic field was applied, nonlinear positive magnetoresistance was detected. A planar topological Hall effect was also identified. The corresponding exponent, $a \approx 1.74$ as shown in Fig. 6(b), indicates that both intrinsic and extrinsic mechanisms contribute in this regime. Lyu *et al.*[22] later combined transport measurements with first-principles calculations to examine the low-temperature AHE. As shown in Fig. 6(c), the intrinsic contribution was found to account for 91.7% of the total AHC. This contribution is associated with Berry curvature hotspots resulting from spin–orbit-coupling-driven anticrossings of electronic bands near the Fermi level. These results show that the interpretation of $PrMn_2Ge_2$ has moved from low-temperature skew scattering to mixed intrinsic/extrinsic behavior and finally to quantitative identification of a dominant intrinsic contribution.

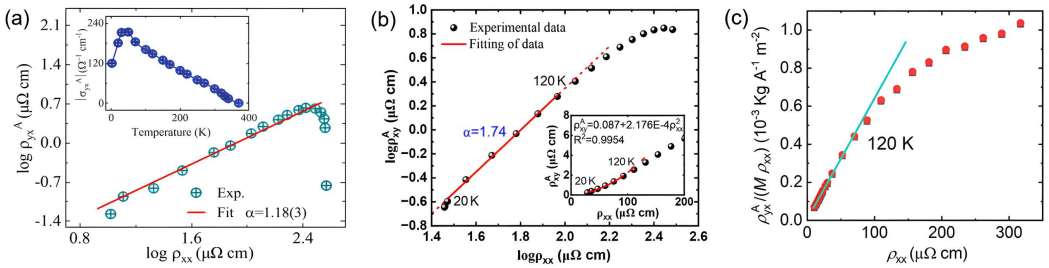

Fig. 6. Evolution of the AHE mechanism in $PrMn_2Ge_2$. (a) Relationship between AHC and temperature;[28] (b) scaling relation between $\log(\rho_{xy}^{A})$ and $\log(\rho_{xx})$;[27] (c) comparison between intrinsic and total anomalous Hall contributions, indicating the dominant role of Berry curvature.[22]

4.4. $NdMn_2Ge_2$

Zheng *et al.*[29] extended the investigation to $NdMn_2Ge_2$ single crystals, and the team measured the Hall response under $I \parallel a$ and $H \parallel c$. As shown in Fig. 7(a), it can be seen that between 220 and 320 K, ρ_{xy}^{A} increases rapidly and saturates in low fields, showing a typical AHE response in this temperature range. At low temperatures, ρ_{xy}^{A} scales linearly with ρ_{xx}, indicating a skew-scattering-dominated regime. At higher temperatures, ρ_{xy}^{A} develops an enhanced broad peak. The available results therefore show how the Hall response in $NdMn_2Ge_2$ evolves across magnetic phases and temperature regimes as shown in Fig. 7(b). Xu *et al.*[32] reported that the AHE in $NdMn_2Ge_2$ does not originate from a single mechanism. The ρ_{yx}/M data can be fitted with both linear and quadratic terms of ρ_{xx}. In addition, the resistivity in the relevant temperature range is about 100–200 μΩ·cm, which argues against skew scattering as the sole dominant contribution. They therefore concluded that the AHE in $NdMn_2Ge_2$ most likely arises from the combined effects of extrinsic skew scattering and an intrinsic Berry curvature related contribution.

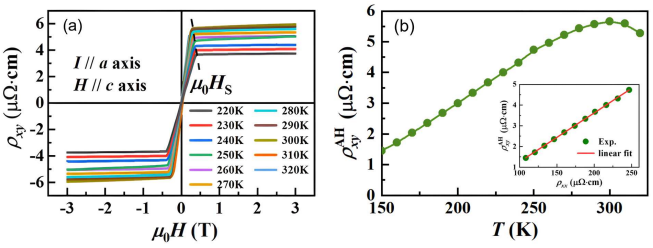

Fig. 7. Hall response in $NdMn_2Ge_2$:[29] (a) magnetic-field-dependent Hall resistivity obtained; (b) temperature-dependent anomalous Hall resistivity and the corresponding linear fit.

4.5. $SmMn_2Ge_2$

Singh *et al.*[36] showed that in the high-temperature phase, under $H \parallel [001]$ and $I \parallel a$, the AHE is completely intrinsic. As shown in Fig. 8(a) in this geometry, σ_{xy}^{A} is about 77–105 $\Omega^{-1}\cdot cm^{-1}$. As presented in Fig. 8(b), the quantity ρ_{yx}^{A}/M_s scales linearly with ρ_{xx}^{2}, yielding an intrinsic component of about 107 $\Omega^{-1}\cdot cm^{-1}$. In the same phase, rotating the field to $H \parallel [010]$ changes the response to an extrinsic skew-scattering regime, with σ_{xz}^{A} reaching 456 $\Omega^{-1}\cdot cm^{-1}$ at 150 K as shown in Fig. 8(c). This contrast shows that the dominant AHE mechanism can be tuned by magnetization direction. At low temperature, the AHE nearly vanishes at 5 K, leaving only

the ordinary Hall effect. As shown in Fig. 8(d), when the temperature is increased to about 50 K and above, the AHE reappears, and σ_{xz}^{A} can rise to 1400 $\Omega^{-1}\cdot cm^{-1}$ under the same magnetization direction.

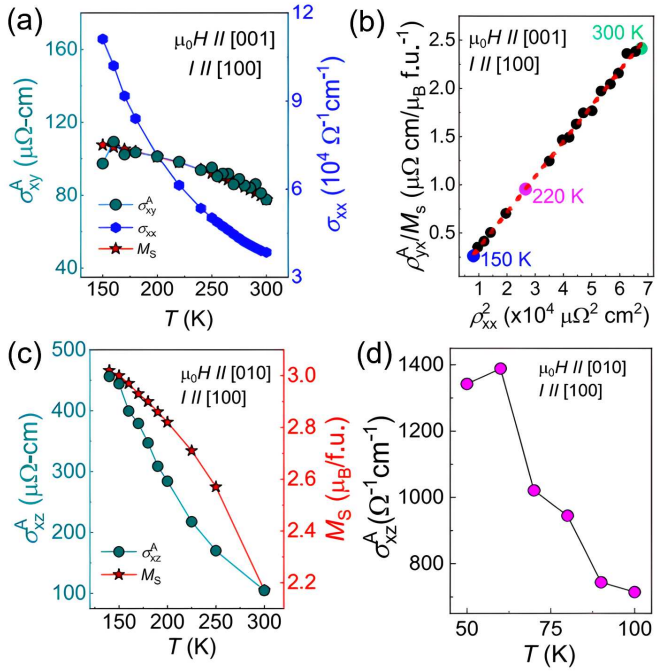

Fig. 8. AHE in $SmMn_2Ge_2$:[36] (a) temperature dependence of AHC; (b) ρ_{yx}^{A}/M_S and ρ_{xx}^{2} showing the scaling relation; (c) temperature dependence of AHC and M_S; (d) AHC.

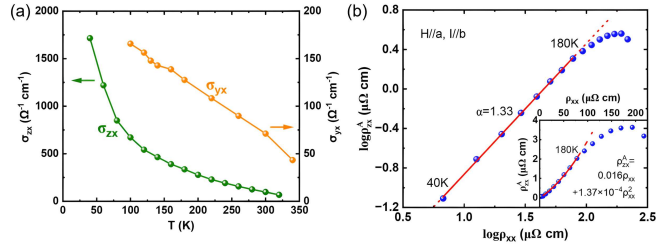

Fig. 9. Giant AHE and scaling behavior in $SmMn_2Ge_2$:[40] (a) temperature dependence of AHC under different magnetic-field directions; (b) scaling relation between $\log(\rho_{xy}^{A})$ and $\log(\rho_{xx})$.

Huang *et al.*[40] also measured σ_{zx} under $H \parallel a$ and $I \parallel b$, obtaining 1715 $\Omega^{-1}\cdot cm^{-1}$ at 40 K as presented in Fig. 9(a), confirming the reproducibility of the giant AHE. By contrast, under $H \parallel c$ and $I \parallel b$, the maximum σ_{xy}^{A} is only about 166 $\Omega^{-1}\cdot cm^{-1}$ at around 100 K. $a = 1.33$ as shown in Fig. 9(b), these findings suggest that the giant AHE for $H \parallel a$ mainly arises from an extrinsic skew-scattering contribution induced by the scalar spin chirality of short-range conical spin clusters, whereas the much smaller AHE for $H \parallel c$ is dominated by an intrinsic mechanism.

The pronounced AHE anisotropy in $SmMn_2Ge_2$ mainly arises from the different contributions of intrinsic Berry curvature and extrinsic scattering mechanisms, both of which are strongly dependent on the magnetization direction. First-principles calculations show that for spin alignment along the c axis, SOC-gapped nodal lines near the Fermi level generate a sizable Berry curvature.[36] In contrast, when spins are aligned along the a axis, these nodal-line states shift above the Fermi level, which strongly suppresses the intrinsic AHE. The scaling analysis suggests that the giant AHE for $H \parallel a$ is predominantly governed by unconventional skew scattering arising from conical Mn spin clusters with scalar spin chirality.[40]

5. ANE and related phenomena in RMn_2Ge_2 ferromagnets

The systematic studies of ANE in light rare-earth RMn_2Ge_2 have mainly focused on $PrMn_2Ge_2$, $NdMn_2Ge_2$, and $SmMn_2Ge_2$. Accordingly, this section does not repeat the concepts and theoretical definitions already introduced in the previous sections, but instead discusses the experimental results, mechanistic criteria, and their connection with the AHE results presented in the previous section for these three materials.

5.1. $PrMn_2Ge_2$

Lyu *et al.*[22] systematically investigated the ANE in $PrMn_2Ge_2$. S_{yx}^{A} as presented in Fig. 10(a), the value reaches 1.16 $\mu V\cdot K^{-1}$ at room temperature and increases to 1.44 $\mu V\cdot K^{-1}$ at 260 K. The α_{yx}^{A} reaches 2.61 A$\cdot$ $m^{-1}\cdot K^{-1}$ under low-temperature conditions. The reported ratio $|S_{yx}^{A}|/M$ is 4.6 $\mu V\cdot K^{-1}\cdot T^{-1}$, which is well above the typical range observed in conventional ferromagnets. This indicates that the ANE in $PrMn_2Ge_2$ cannot be accounted for solely by the macroscopic magnetic moment. As shown in Fig. 10(b),

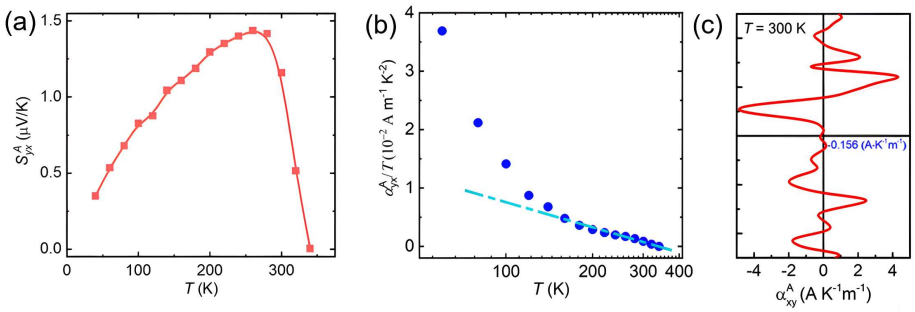

Fig. 10. ANE and Berry curvature mechanism in $PrMn_2Ge_2$:[22] (a) temperature-dependent behavior of the anomalous Nernst signal; (b) temperature scaling behavior of α_{yx}^{A}/T; (c) α_{xy}^{A} profile in the vicinity of the Fermi level.

with respect to temperature dependence, α_{yx}^{A} exhibits $T\ln T$ scaling above 150 K but increases rapidly at lower temperatures, deviating from this relation. As shown in Fig. 10(c), theoretical analysis based on first-principles calculations with SOC taken into account, combined with a Wannier tight-binding model, reveals pronounced Berry curvature hot spots near the Fermi level. The calculated α_{yx}^{A} agrees well with experimental data, confirming that the ANE is predominantly intrinsic and driven by Berry curvature.

5.2. $NdMn_2Ge_2$

Xu *et al.*[32] reported the ANE in $NdMn_2Ge_2$ single crystals. As shown in Fig. 11(a), $|S_{xy}^{A}|$ reaches 1.4 $\mu V\cdot K^{-1}$, mainly in the canted antiferromagnetic and conical phases with a substantial out-of-plane ferromagnetic component. The α_{yx}^{A} is expressed as: $\alpha_{yx}^{A} = \sigma_{xx}S_{xy}^{A} + \sigma_{xy}^{A}S_{xx}$. α_{xy}^{A} increases upon cooling, reaching 0.6 $A\cdot m^{-1}\cdot K^{-1}$ at 160 K as shown in Fig. 11(b). The two contributions, $\sigma_{xx}S_{xy}^{A}$ and $\sigma_{xy}^{A}S_{xx}$, have opposite signs, indicating multicomponent coupling in the anomalous transverse transport. The ANE in $NdMn_2Ge_2$ was interpreted by the authors as arising from combined contributions of skew scattering and the Berry curvature of electronic bands, rather than a single mechanism.

5.3. $SmMn_2Ge_2$

Yan *et al.*[41] reported a pronounced ANE in $SmMn_2Ge_2$ single crystals. As shown in Fig. 12(a), S_{yx}^{A} reaches 1.04 $\mu V/K$ at room temperature, with an anomalous Nernst angle (ANA) of 11%. The corresponding transverse thermoelectric figure of merit, zT_{ANE}, is 5×10^{-5}. As shown in Fig. 12(b), based on the comparison of $|S_{yx}^{A}|$ with $\mu_0 M$, the anomalous Nernst coefficient Q_s is 2.97 $\mu V\cdot K^{-1}\cdot T^{-1}$, exceeding the typical empirical range for conventional ferromagnets. Decomposition analysis shows that α_{yx}^{A} reaches 0.27 $A\cdot m^{-1}\cdot K^{-1}$ at 290 K. The two contributions have opposite signs, with the first term dominant. α_{yx}^{A} follows $T\ln T$ scaling at above 280 K and approaches a linear temperature dependence at below 280 K as shown in Fig. 12(c). These results indicate that the ANE in $SmMn_2Ge_2$ is predominantly intrinsic and governed by Berry curvature. Taken together, $SmMn_2Ge_2$ exhibits a large S_{yx}^{A}, a high ANA, and considerable transverse thermoelectric performance at room temperature. Its anomalous transverse thermoelectric transport originates predominantly from intrinsic Berry curvature.

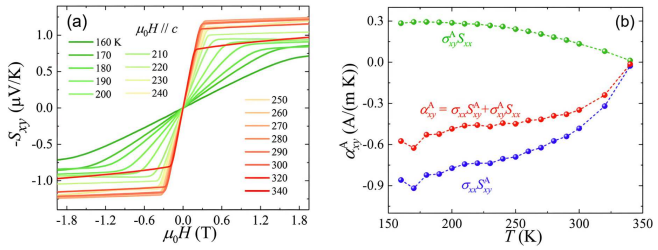

Fig. 11. ANE and decomposition of transverse thermoelectric transport in $NdMn_2Ge_2$:[32] (a) Nernst signal measured at different temperatures as a function of magnetic field; (b) temperature dependence of α_{yx}^{A} and its two contributing terms.

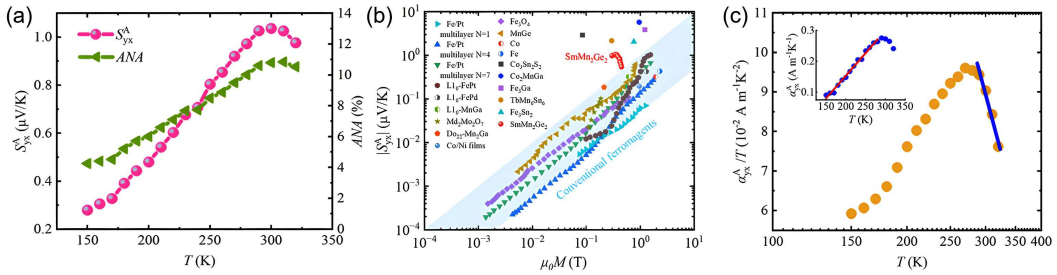

Fig. 12. Room-temperature ANE and Berry curvature mechanism in $SmMn_2Ge_2$:[41] (a) temperature-dependent behavior of the anomalous Nernst signal and ANA; (b) scaling relation between $|S_{yx}^{A}|$ and $\mu_0 M$; (c) temperature scaling behavior of α_{yx}^{A}/T.

6. Conclusion and perspectives

In summary, light rare-earth RMn_2Ge_2 compounds represent an ideal platform for studying anomalous transverse transport in layered magnetic systems. The results reviewed here indicate that the AHE and ANE in these compounds are primarily attributable to the Mn-3d electronic states. Consistently, $LaMn_2Ge_2$ exhibits a pronounced intrinsic AHE even in the absence of localized 4f magnetic moments.[9,10] The rare-earth 4f electrons modulate the relative contributions of intrinsic Berry curvature and extrinsic scattering mechanisms via 4f–3d exchange coupling, magnetic anisotropy, Mn-spin reorientation, etc. For example, the intrinsic AHE contribution is approximately 81% in $CeMn_2Ge_2$[17] and 91.7% in $PrMn_2Ge_2$.[22] Further work combining transport measurements, magnetic-structure characterization, and first-principles calculations under well-defined measurement conditions will be crucial for elucidating the dominant mechanisms in this family. In addition, systematic studies on disorder, strain, pressure, chemical substitution, and reduced dimensionality may provide further insights into, and facilitate control over, the anomalous transverse transport properties of RMn_2Ge_2 compounds.

Acknowledgements

This work was sponsored by Zhejiang Provincial Natural Science Foundation of China (Grant No. LD24F040001)

and the National Natural Science Foundation of China (Grant Nos. 52371244 and U23A20551).

References

[1] Nagaosa N, Sinova A, Onoda S, MacDonald A H and Ong N P 2010 *Rev. Mod. Phys.* **82** 1539
[2] Xiao D, Chang M C and Niu Q 2010 *Rev. Mod. Phys.* **82** 1959
[3] Hou Q Y, Song M, Xu X T, Wang Y H, Dong C, Feng Y F, He M, Liu Y L, Cao L, Wang J F, Qu Z and Xiong Y M 2023 *Chin. Phys. B* **32** 087501
[4] Wang X Y, Lin J F, Zeng X Y, Wang H, Ma X P, Wang Y T, Han K and Xia T L 2023 *Chin. Phys. Lett.* **40** 067503
[5] Yang X Y, Zeng Q Q, He M, Xu X T, Du H F and Qu Z 2024 *Chin. Phys. B* **33** 077501
[6] Wang X X, Wang W Q, Hutchison W D, Wang C W, Hao H Y, Su F, Xue Y F, Debnath J C, Campbell S J, Cheng Z X and Wang J L 2022 *J. Alloys Compd.* **909** 164784
[7] Welter R, Venturini G, Ressouche E and Malaman B 1995 *J. Alloys Compd.* **218** 204
[8] Tomka G J, Ritter C, Riedi P C, Kapusta C Z and Kocemba W 1998 *Phys. Rev. B* **58** 6330
[9] Gong G S, Xu L M, Bai Y M, Wang Y Q, Yuan S L, Liu Y and Tian Z M 2021 *Phys. Rev. Mater.* **5** 034405
[10] Roychowdhury S, Yanda P, Samanta K, Yi C J, Yao M Y, Orlandi F, Manuel P, Khalyavin D, Della Valle E G, Constantinou P, Strocov V N, Vergniory M G, Shekhar C and Felser C 2024 *Adv. Mater.* **36** 2305916
[11] Chen Y C, Li F, Jin S Z, Liu Y J, Zhang H Y, Nie H, Zhang L Y and Wang X Y 2025 *J. Alloys Compd.* **1017** 179156
[12] Shigeoka T, Iwata N, Fujii H and Okamoto T 1985 *J. Magn. Magn. Mater.* **53** 83
[13] Jammalamadaka S N, Das S D, Chalke B A and Sampathkumaran E V 2008 *J. Magn. Magn. Mater.* **320** L129
[14] Di Napoli S, Bihlmayer G, Blügel S, Alouani M, Dreyssé H and Llois A M 2004 *J. Magn. Magn. Mater.* **272** E265
[15] Venturini G, Welter R, Ressouche E and Malaman B 1994 *J. Alloys Compd.* **210** 213
[16] Narasimhan K S V L, Rao V U S, Bergner R L and Wallace W E 1975 *J. Appl. Phys.* **46** 4957
[17] Xu L M, Bai Y M, Gong G S, Song F Y, Li Z H, Han Y Y, Ling L S and Tian Z M 2022 *Phys. Rev. B* **105** 075108
[18] Wang S Y, Ma L, He L D, Liu D M, Wang Y B, Fan C Z, Liu E K and Wang C 2024 *Inorg. Chem.* **63** 24834
[19] Xu G L, Liu D M, He L D, Wang S B and Ma L 2022 *Mater. Lett.* **315** 131963
[20] Fernandez-Baca J A, Hill P, Chakoumakos B C and Ali N 1996 *J. Appl. Phys.* **79** 5398
[21] Lalić M V, Mestnik-Filho J, Carbonari A W and Saxena R N 2004 *J. Phys. Condens. Matter* **16** 6685
[22] Lyu M, Liu J Y, Zhang S, Liu Y, Yang J Y, Wang Y B, Feng Y T, Wang B B, Wei H X and Liu E K 2025 *Phys. Rev. B* **111** 014424
[23] Song M, Zhao J, Liu C X, He M, Wang Y H, Han Y Y, Ling L S, Cao L, Zhang L, Qu Z and Xiong Y M 2022 *Appl. Phys. Lett.* **120** 092402
[24] Bosch S B, Cabrera P G A, Saxena R N, Freitas R S and Carbonari A W 2017 *AIP Adv.* **7** 056211
[25] Li J Y, Hao H Y, Hutchison W D, Hu C C, Su F, Xue Y F, Gu Q F, Campbell S J, Wang W Q, Cheng Z X and Wang J L 2024 *Intermetallics* **168** 108270
[26] Wang J L, Campbell S J, Hofmann M, Kennedy S J, Avdeev M, Md Din M F, Zeng R, Cheng Z X and Dou S X 2013 *J. Appl. Phys.* **113** 17E147
[27] Huang D, Li H, Ding B, Xi X K, Lau Y C and Wang W H 2023 *Phys. Rev. B* **107** 224417
[28] Wang X Y, Xu S, Wang H, Lin J F, Zeng X Y, Ma X P, Gong J, Wang Y T, Han K and Xia T L 2023 *Phys. Rev. B* **107** 144402
[29] Zheng X, Zhao X W, Qi J, Luo X H, Ma S C, Chen C C, Zeng H, Yu G, Fang N, Rehman S U, Ren W J, Li B and Zhong Z C 2021 *Appl. Phys. Lett.* **118** 072402
[30] Ye P, Xin W, De Rosa I M, Wang Y, Goorsky M S, Zheng L, Yin X and Xie Y-H 2020 *ACS Appl. Mater. Interfaces* **12** 22050
[31] Zhao J, Zhao K, Gao C, Zeng Z, Rahman A, Qin Y, Chen L, Ren W, Gao H, Qu Z and Zhang L 2026 *Mater. Res. Lett.* **14** 312
[32] Xu C, Tian W, Zhang P and Ke X 2023 *Phys. Rev. B* **108** 064430
[33] Tomka G J, Kapusta C, Ritter C and Riedi P C 1998 *J. Magn. Magn. Mater.* **177** 821
[34] Bosch-Santos B, Carbonari A W, Cabrera-Pasca G A, Saxena R N and Freitas R S 2015 *J. Appl. Phys.* **117** 17E304
[35] Wang S B, Zeng Q W, Liu D M, Zhang H G, Ma L, Xu G L, Liang Y T, Zhang Z L, Wu H, Che R C, Han X D and Huang Q Z 2020 *ACS Appl. Mater. Interfaces* **12** 24125
[36] Singh M, Sau J, Rai B, Panda A, Kumar M and Kumar N 2024 *Phys. Rev. Mater.* **8** 084201
[37] Fujii H, Okamoto T, Shigeoka T and Iwata N 1985 *Solid State Commun.* **53** 715
[38] Duraj M, Duraj R, Szytuła A and Tomkowicz Z 1988 *J. Magn. Magn. Mater.* **73** 240
[39] Koyama K, Miura S, Okada H, Shigeoka T, Fujieda S, Fujita A, Fukamichi K and Watanabe K 2006 *J. Alloys Compd.* **408** 118
[40] Huang D, Li H, Ding B, Song L X, Li X, Xi X K, Lau Y C, Gao J R and Wang W H 2024 *Phys. Rev. B* **109** 144406
[41] Yan B Y, Liu L F, Wang H Y, Yan T, Tang Y Z, Chen C Y, Li W and Wang B M 2026 *Appl. Phys. Lett.* **128** 072401
[42] Reichlova H, Janda T, Godinho J, Markou A, Kriegner D, Schlitz R, Zelezny J, Soban Z, Bejarano M, Schultheiss H, Nemec P, Jungwirth T, Felser C, Wunderlich J and Goennenwein S T B 2019 *Nat. Commun.* **10** 5459
[43] Zhou X D, Hanke J P, Feng W X, Blügel S, Mokrousov Y and Yao Y G 2020 *Phys. Rev. Mater.* **4** 024408
[44] Jungwirth T, Abolfath M, Sinova J, Kučera J and MacDonald A H 2002 *Appl. Phys. Lett.* **81** 4029
[45] Xu Z A, Yuan J, Yan Z, Wang X, Yu N, Zhang S H and Guo Y F 2026 *Chin. Phys. Lett.* **43** 060705
[46] Chang M C and Niu Q 1996 *Phys. Rev. B* **53** 7010
[47] Mainkar N, Browne D A and Callaway J 1996 *Phys. Rev. B* **53** 3692
[48] Smit J 1958 *Physica* **24** 39
[49] Berger L 1970 *Phys. Rev. B* **2** 4559
[50] Beckert S, Godinho J, Johnson F, Kimák J, Schmoranzerová E, Zemen J, Šobáň Z, Olejník K, Železný J, Wunderlich J, Němec P, Kriegner D, Thomas A, Goennenwein S T B, Cohen L F and Reichlová H 2023 *Phys. Rev. B* **108** 024420
[51] Fujikawa K and Umetsu K 2023 *Prog. Part. Nucl. Phys.* **128** 103992
[52] Mizuguchi M and Nakatsuji S 2019 *Sci. Technol. Adv. Mater.* **20** 262
[53] Onoda S, Sugimoto N and Nagaosa N 2006 *Phys. Rev. Lett.* **97** 126602
[54] Noky J, Zhang Y, Gooth J, Felser C and Sun Y 2020 *npj Comput. Mater.* **6** 77